

Emission-based estimation of lung attenuation coefficients for attenuation correction in time-of-flight PET/MR

Abolfazl Mehranian¹ and Habib Zaidi^{1,2,3}

¹ Division of Nuclear Medicine and Molecular Imaging, Geneva University Hospital, CH-1211, Geneva, Switzerland

² Geneva Neuroscience Centre, University of Geneva, CH-1205, Geneva, Switzerland

³ Department of Nuclear Medicine and Molecular Imaging, University of Groningen, Groningen, The Netherlands

E-mail: habib.zaidi@hcuge.ch

Received 20 November 2014, revised 2 April 2015

Accepted for publication 28 April 2015

Published 5 June 2015



CrossMark

Abstract

In standard segmentation-based MRI-guided attenuation correction (MRAC) of PET data on hybrid PET/MRI systems, the inter/intra-patient variability of linear attenuation coefficients (LACs) is ignored owing to the assignment of a constant LAC to each tissue class. This can lead to PET quantification errors, especially in the lung regions. In this work, we aim to derive continuous and patient-specific lung LACs from time-of-flight (TOF) PET emission data using the maximum likelihood reconstruction of activity and attenuation (MLAA) algorithm. The MLAA algorithm was constrained for estimation of lung LACs only in the standard 4-class MR attenuation map using Gaussian lung tissue preference and Markov random field smoothness priors. MRAC maps were derived from segmentation of CT images of 19 TOF-PET/CT clinical studies into background air, lung, soft tissue and fat tissue classes, followed by assignment of predefined LACs of 0, 0.0224, 0.0864 and 0.0975 cm⁻¹, respectively. The lung LACs of the resulting attenuation maps were then estimated from emission data using the proposed MLAA algorithm. PET quantification accuracy of MRAC and MLAA methods was evaluated against the reference CT-based AC method in the lungs, lesions located in/near the lungs and neighbouring tissues. The results show that the proposed MLAA algorithm is capable of retrieving lung density gradients and compensate fairly for respiratory-phase mismatch between PET and corresponding attenuation maps. It was found that the mean of the estimated lung LACs generally follow the trend of the reference CT-based attenuation correction (CTAC) method. Quantitative analysis revealed that the MRAC method resulted in average relative errors of $-5.2 \pm 7.1\%$ and $-6.1 \pm 6.7\%$ in the lungs and lesions,

respectively. These were reduced by the MLAA algorithm to $-0.8 \pm 6.3\%$ and $-3.3 \pm 4.7\%$, respectively. In conclusion, we demonstrated the potential and capability of emission-based methods in deriving patient-specific lung LACs to improve the accuracy of attenuation correction in TOF PET/MR imaging, thus paving the way for their adaptation in the clinic.

Keywords: TOF, PET/MRI, attenuation correction, quantification, lung attenuation

(Some figures may appear in colour only in the online journal)

1. Introduction

Hybrid positron emission tomography/magnetic resonance imaging (PET/MRI) technology combines the physiological and metabolic information provided by PET with the structural and functional information provided by MRI. Over the last decade, this hybrid imaging modality attracted a great deal of attention and many efforts have been directed towards addressing the challenges encountered in system design and quantitative imaging, thus paving the way to explore its potential and clinical applications (Torigian *et al* 2013, Disselhorst *et al* 2014). In this context, attenuation correction (AC) is one of the major challenges facing quantitative PET/MR imaging (Zaidi 2007, Bezrukov *et al* 2013a).

In contrast to x-ray computed tomography (CT), the MRI signal is correlated with hydrogen proton density, relaxation time properties of tissues and the selected pulse timing parameters, rather than electron density. As such, there is no straightforward approach to directly map MR image intensities to PET 511 keV attenuation coefficients as in PET/CT. Several approaches have been proposed for attenuation correction in PET/MR including (i) MRI-based attenuation map generation (MRAC), (ii) transmission measurements and (iii) emission based estimation of PET linear attenuation coefficients (LACs). In the first category of methods, MR images are either segmented into several tissue classes followed by assignment of predefined attenuation coefficients to each class (Martinez-Moller *et al* 2009, Hu *et al* 2010) or used to generate pseudo-CT images through atlas registration and machine learning techniques (Hofmann *et al* 2008, Schreiber *et al* 2010, Johansson *et al* 2011, Marshall *et al* 2013, Navalpakkam *et al* 2013). In fast gradient-echo MR pulse sequences, usually used to acquire whole-body MRAC maps, cortical and spongy bones cannot be well discriminated from air and surrounding soft tissues owing to their low water content and short transverse relaxation time. Therefore, bones are either replaced by soft tissue or predicted by pseudo-CT generation techniques. MRI field-of-view truncation and metal-induced magnetic susceptibility artefacts are other limitations that need to be addressed when using this category of methods.

The second category of methods measures directly the LACs using external positron-emitting sources (Mollet *et al* 2014) or background radiation of LSO crystals (Rothfuss *et al* 2014) for simultaneous emission/transmission acquisition in time-of-flight (TOF) PET/MRI. In these revisited transmission-based attenuation correction methods, the time-of-flight information is used to separate the emission data from transmission. The major issue is the low count statistics of the transmission scan limited by the emission scan time per bed position. In consequence, the measured attenuation maps might suffer from noise and introduce additional noise and bias in the emission maps.

The last approach consists in estimating attenuation information directly from the emission data. In this category of techniques, the attenuation coefficients or attenuation sinograms are estimated either without reconstruction of the activity map, based on the Helgason–Ludwig

consistency conditions of the attenuated Radon transform (Welch *et al* 1998, Bronnikov 2000, Kacperski 2011, Defrise *et al* 2012), or with simultaneous maximum likelihood reconstruction of activity and attenuation (MLAA) or attenuation correction factors (MLACF) (Nuyts *et al* 1999, Krol *et al* 2001, Landmann *et al* 2002, Rezaei *et al* 2014). According to consistency conditions, a given noise-free emission data only arises under certain attenuation conditions and vice versa. These conditions do not model the statistical variability of the emission data and generally cannot uniquely estimate attenuation information. However, based on the range consistency conditions of TOF attenuated Radon transform, Defrise *et al* (Defrise *et al* 2012) recently showed that attenuation correction factors can be uniquely determined from PET TOF data up to a constant scaling factor. In the maximum likelihood framework, the statistical nature of the data is properly modelled; however, the estimated activity and attenuation maps or attenuation correction factors are not unique and often suffer from cross talk artefacts, where the features of the activity map propagates into the attenuation map and vice versa. With the advent of TOF PET/MRI scanners, Salomon *et al* imposed MR anatomical information on the TOF-MLAA estimation of attenuation coefficients (Salomon *et al* 2009). Thereby, the noise and cross-talk artefacts were considerably reduced. Later, Rezaei *et al* demonstrated that the inherent spatial constraint of TOF-PET data suppresses the cross-talks in the simultaneous reconstruction of activity and attenuation (Rezaei *et al* 2012). However, the activity maps are globally scaled and the attenuation maps present with a position-dependent scaling. Aside from the scale problem, the performance of MLAA algorithms depends on TOF timing resolution, emission count statistics and the spatial distribution of the radiotracer, which supports the estimation of attenuation coefficients. More recently, the combination of transmission- and emission-based approaches has been explored in the joint estimation of activity and attenuation using rotating rod (Panin *et al* 2013) or sparse point transmission sources (Watson 2014). This combination could circumvent the shortcomings of standalone transmission- and emission-based methods.

Current commercial PET/MRI systems employ segmentation-based MRAC for attenuation correction of PET data. In these methods, MR images are segmented into three or four tissue classes, namely background air, lung, fat and non-fat soft tissues, followed by assignment of constant LACs to each tissue class. Overall, these techniques were reported to result in PET quantification bias in terms of standardized uptake value (SUV) of <5% in most soft tissue lesions (Martinez-Moller *et al* 2009, Schulz *et al* 2011). However, the substitution of bones by soft tissue can lead to SUV errors ranging from 8 to 27% in bony structures (Martinez-Moller *et al* 2009, Arabi *et al* 2015). Moreover, inter/intra-patient heterogeneity of attenuation coefficients in different tissue classes is ignored, which can lead to a high variance of SUV errors, especially in the lungs. The determination of patient-specific lung LACs is a challenging task, since the pulmonary parenchyma and vasculature and thus lung LACs vary considerably among patients by as much as 30%, depending on gender, body height, pathological conditions (Karimi *et al* 2014), breathing patterns (Robinson and Kreel 1979) and body positioning (Gattinoni *et al* 1991). As such, different attenuation coefficients have been assigned to lung tissue class, ranging from 0.018 to 0.035 cm⁻¹ (Martinez-Moller *et al* 2009, Kim *et al* 2012). In addition, the mis-segmentation of soft tissue lesions, specifically in the mediastinal sides of the lungs, can lead to substantial lesion quantification errors.

A limited number of studies focused on the derivation of patient-specific lung attenuation coefficients in segmentation-based MRAC methods. Marshall *et al* established a linear mapping function between MRI and CT image intensities of the lungs in order to predict the mean of lung LACs for each patient (Marshall *et al* 2012). Lonn *et al* (Lonn and Wollenweber 2012) derived a linear relationship between lung volume and mean LACs for the prediction of mean lung attenuation coefficients. Overall, the MRI-to-CT mapping function requires a

standardized MRI protocol and is influenced by the presence of diamagnetic susceptibility and flow-related artefacts. Moreover, the volume-to-LAC prediction model does not take into account the impact of factors, such as gender, age, pathological conditions and body positioning. Emission-based derivation of lung LACs has also been explored. Madsen and Lee used the consistency conditions to refine an initial lung contour obtained from a lung atlas and the MLAA framework to estimate the attenuation coefficients (Madsen and Lee 1999). Recently, Berker *et al* explored a constrained TOF-MLAA algorithm for the estimation of mean lung LACs in 5-class MRAC maps (including bones as 5th class) (Berker *et al* 2012). The results obtained using Monte Carlo simulated PET/CT studies showed a high bias in PET quantification, possibly because of out-of-field accidental coincidences, error propagation into the lungs and the unsolved scaling problem of the MLAA algorithm.

More recently, we proposed an approach to improve the performance of the MLAA algorithm by incorporating MRI spatial and CT statistical information in the joint estimation of activity and attenuation using a mixture of Gaussian model (Mehranian and Zaidi 2015a). In this approach, a continuous attenuation map is estimated from the emission data under the constraint of a multi-class Gaussian prior with suppression of cross-talk and scale problems. In the current work, we simplified this algorithm to only estimate lung attenuation coefficients in the 4-class MRI-guided attenuation correction of clinical studies with the aim of demonstrating the potential of emission-based AC methods in deriving patient-specific lung LACs, thus paving the way for a smooth translation of these methods into clinical TOF PET/MR imaging.

2. Material and methods

2.1. Constrained MLAA

In TOF-PET, the statistical variability of measured data, g_{it} in a line-of-response (LOR) i and TOF bin t is best modelled by a Poisson distribution with expected value:

$$\bar{g}_{it} = n_i a_i \sum_{j=1}^J c_{ijt} \lambda_j + n_i \bar{s}_{it} + \bar{r}_{it} \quad (1)$$

where λ_j denote activity values at voxel j , C_{ijt} is the geometric probability detection of annihilation events emitted from voxel j along LOR i in TOF bin t , n_i are detector normalization factors, a_i is attenuation survival probability of annihilation photons along LOR i , \bar{s}_{it} is the model-based expected estimate of scatter coincidences and \bar{r}_{it} is the expected value of random coincidences, obtained by smoothing the measurements of a delayed coincidence window. In this work, only the lung attenuation coefficients of 4-class MR attenuation maps are assumed to be unknown, therefore, a_i can be decomposed into the product of known and unknown attenuation factors (Nuyts *et al* 2013):

$$a_i = \exp\left(-\sum_{k \notin \mathbb{L}} l_{ik} \mu_k\right) \exp\left(-\sum_{k \in \mathbb{L}} l_{ik} \mu_k\right) \quad (2)$$

where μ_k and l_{ik} are attenuation values of voxel k and the intersection length of LOR i with voxel k . \mathbb{L} is the set of all voxels belonging to the lungs, obtained from segmentation of MR images. The lung attenuation coefficients can therefore be estimated using the following joint maximum *a posteriori* estimation of activity and attenuation:

$$\begin{aligned}
 (\hat{\lambda}, \hat{\mu}) = \operatorname{argmax}_{\lambda \geq 0, \mu \geq 0} & \left\{ \sum_{it} \{g_{it} \log(\bar{g}_{it}) - \bar{g}_{it}\} - \frac{\beta}{2} \sum_{j \in \mathbb{L}} \sum_{k \in N_j} \omega_{jk} (\mu_k - \mu_j)^2 \right. \\
 & \left. - \frac{\gamma}{2} \sum_{j \in \mathbb{L}} \left(\frac{\mu_j - \bar{\mu}}{\sigma} \right)^2 \right\} \quad (3)
 \end{aligned}$$

where the objective function consists of the following terms: the Poisson log-likelihood of the measurements, a Markov random field (MRF) smoothing prior and a Gaussian tissue preference. Since the joint tomographic image reconstruction problem is highly ill-posed, it is necessary to constrain the solution space by favouring smooth solutions and penalizing the estimates inconsistent with our expectations. The quadratic MRF prior in equation (3) favours the attenuation maps that are smooth based on the local interactions of each voxel j with its neighbouring voxels in the neighbourhood N_j . In this study, a second-order neighbourhood was used around the j th voxel with 26 nearest neighbours. ω_{jk} is inversely proportional to the distance between voxels j and k . The hyper-parameters β and γ are defined for weighting the impact of the priors. In this study, the Gaussian prior is a uni-modal function centred at the expected value, $\bar{\mu}$, of lung attenuation coefficients obtained from a patient population. Based on the modelled standard deviation, σ , of the LACs and the strength of the γ parameter, this Gaussian lung preference prior penalizes the large variation of the estimated lung LACs from their expected value.

2.2. Optimization

The joint estimation problem defined in equation (2) is not necessarily strictly concave (Clinthorne *et al* 1991), therefore finding a global maximizer is not guaranteed. Since the activity and attenuation are coupled in this problem, an alternating iterative optimization approach is used to reach at least a (strict) local minimizer. As in the joint alternate-maximize (JAM) (Clinthorne *et al* 1991) and MLAA (Nuyts *et al* 1999, Rezaei *et al* 2012) algorithms, at each iteration, maximization is performed with respect to activity (λ -step) while keeping the attenuation constant and then with respect to attenuation (μ -step) with the most recent estimate of activity. In the λ -step, the problem is reduced to an emission maximum likelihood optimization problem that can be solved using a conventional TOF ordinary Poisson ordered subset expectation maximization (OP-OSEM) algorithm. In the μ -step, the problem is reduced to a transmission maximum *a posteriori* optimization problem that can be solved using an ordered subset separable paraboloidal surrogates (OS-SPS) or maximum likelihood for transmission tomography (OS-MLTR) algorithms. MLTR uses De Pierro's additive convexity and Jensen inequality to define an easy-to-optimize surrogate for the transmission log-likelihood function (Fessler *et al* 1997, Nuyts *et al* 1998). The MRF and Gaussian priors are strictly concave functions; therefore the resulting problem can be easily optimized.

The resulting alternating optimization algorithm at the n th global iteration consists of four main steps defined by equations (4)–(7). First, the attenuation survival factors are calculated from the current attenuation map. At the first iteration, they are derived from the initial 4-class MRAC map. The activity is then estimated using a TOF-OPOSEM with several sub-iterations. In the next step, the total activity ψ_i along LOR i is calculated from the estimated activity to serve as the blank scan in the following transmission reconstruction by the non-TOF forward projection of the activity and normalizing and attenuating the resulting sinograms. Finally, the

attenuation map is updated using a non-TOF OS-MLTR algorithm with several sub-iterations only over the lungs using the function δ .

$$a_i^n = e^{-\sum_j l_{ij}\mu_j^n} \tag{4}$$

$$\lambda_j^{n+1} = \frac{\lambda_j^n}{\sum_i c_{ij}n_i a_i^n} \sum_{it} c_{ijt}n_i a_i^n \frac{g_{it}}{n_i a_i^n \sum_{kt} c_{ikt}\lambda_k^n + n_i \bar{s}_{it} + \bar{r}_{it}} \tag{5}$$

$$\psi_i^n = n_i a_i^n \sum_{jt} c_{ijt}\lambda_j^{n+1} \tag{6}$$

$$\mu_j^{n+1} = \mu_j^n + \alpha \delta_j \left(\frac{\sum_i l_{ij} \frac{\psi_i^n}{\psi_i^n + b_i} (\psi_i^n + b_i - g_i) - \gamma \frac{\mu_j^n - \bar{\mu}}{\sigma^2} - \beta \frac{\partial R_{\text{MRF}}(\mu^n)}{\partial \mu_j}}{\sum_j l_{ij} \frac{(\psi_i^n)^2}{\psi_i^n + b_i} \sum_k l_{ik} - \frac{\gamma}{\sigma^2} + \beta \frac{\partial^2 R_{\text{MRF}}(\mu^n)}{\partial^2 \mu_j}} \right) \tag{7}$$

where $b_i = n_i \bar{s}_i + \bar{r}_i$ are background counts in LOR i , $c_{ij} = \sum_t c_{ijt}$, $g_i = \sum_t g_{it}$, $\bar{s}_i = \sum_t \bar{s}_{it}$ and $\bar{r}_i = \sum_{it} \bar{r}_{it}$ are TOF-integrated quantities, $\alpha > 0$ is a step size parameter. R_{MRF} is the MRF quadratic smoothing prior defined in equation (3). For the lung set \mathbb{L} , δ_j is defined as:

$$\delta_j = \begin{cases} 1, & j \in \mathbb{L} \\ 0, & j \notin \mathbb{L} \end{cases} \tag{8}$$

Figure 1(A) illustrates schematically the flowchart of the MLAA algorithm, which alternates between λ -step (OSEM) and μ -step (OS-MLTR) with n global iterations. In this study, we used 15 global iterations, one iteration and two subsets for the λ -step and one iteration and three subsets for μ -step. The activity was uniformly initialized inside the reconstruction field-of-view (FOV), while the attenuation was initialized by an initial 4-class MR-based attenuation map and only updated for voxels belonging to the lungs. As discussed in section 2.5, in this work, MR attenuation maps were derived from CT images. For both OSEM and OS-MLTR reconstructions, the scatter component is estimated using the initial MRAC map and TOF single scatter simulation algorithm implemented in Siemens VG50 e7 tool. Following the update of the lung attenuation coefficients after n global iterations of the constrained MLAA algorithm, the final PET activity map is reconstructed using the standard clinical image reconstruction protocol using the updated attenuation and a new scatter estimate. Figure 1(B) summarizes the reconstruction procedure followed in this study. As discussed in the Results section, we experimentally set the involved hyper-parameters to $\alpha = 1.5$, $\beta = 80$, $\gamma = 0.75$ for all clinical datasets.

2.3. Data acquisition and image reconstruction

Clinical PET/CT studies were acquired on the Biograph mCT Flow Edge 128 scanner (Siemens Healthcare, Erlangen). The PET component of the scanner consists of four rings of 48 detector blocks, each containing 13×13 LSO crystals with dimensions of $4 \times 4 \times 20 \text{ mm}^3$ (total number of 32448 physical crystals). Considering the gaps between block rings, this configuration results in 55 crystal rings covering an axial FOV of 218mm and a transaxial FOV of 700mm. PET data were acquired with maximum ring difference of 49 planes in continuous

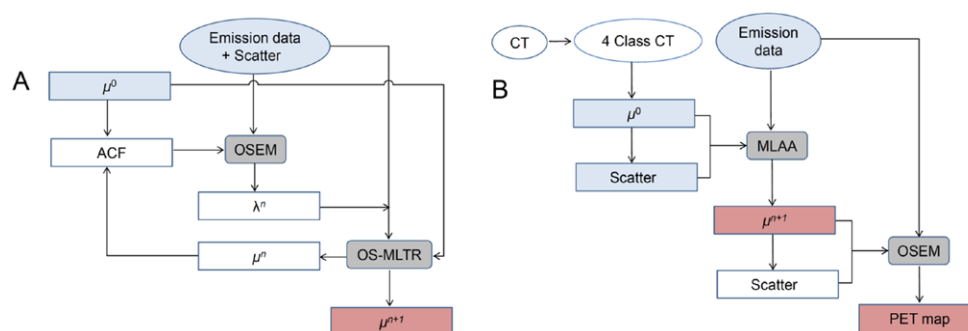


Figure 1. (A) Flowchart of the MLAA algorithm, which alternates between an OSEM activity reconstruction and an OS-MLTR attenuation reconstruction. (B) Flowchart of the whole procedure followed in this study. First, the CT images are segmented into 4-class attenuation maps, representing standard 4-class MRAC maps. Then the MLAA algorithm is initialized by the MRAC attenuation and corresponding scatter sinograms. In the next step, the estimated attenuation maps are used for an ordinary OSEM reconstruction with the parameters used in clinical setting.

bed motion (CBM) mode. The coincidence window width is 4.06 ns with an effective TOF timing resolution of 580 ps. PET images were reconstructed using Siemens VG50 e7 tool with an OP-OSEM algorithm, incorporating all corrections (scatter, random, dead time, decay, attenuation, and normalization) into the reconstruction procedure, with point spread function (PSF) modelling and TOF information. The default manufacturer-provided reconstruction parameters for OSEM + PSF + TOF were used (two iterations and 21 subsets). The single-bed image matrix size is $200 \times 200 \times 109$ with $4 \times 4 \times 2 \text{ mm}^3$ voxels. For the joint reconstruction of activity and lung attenuation values, an in-house TOF PET image reconstruction software was developed for the native geometry of the mCT scanner. The list-mode data of the scanner are histogrammed in 4D sinograms with 400 radial bins, 168 azimuthal angles, 621 planes (in 9 segments with span 11) and 13 time bins of 312.5 ps width. The MLAA images were reconstructed using a matrix size of $200 \times 200 \times 109$ per bed. For large axial FOVs, the data acquired in CBM mode are chunked into conventional bed positions, which are then reconstructed separately. In this work, we selected the bed positions that axially covered the whole lungs (usually one or two beds). After the MLAA estimation of attenuation maps, the corresponding attenuation maps were assembled and the final activity images were reconstructed using the e7 tools.

2.4. Clinical studies

In this retrospective study, a total number of 19 patients (eight women, 11 men; average age 56.5 ± 19.7 years), who underwent ^{18}F -FDG ($n = 17$) and ^{18}F -Choline ($n = 2$) PET/CT examinations, were included and analyzed. The clinical indications of the examinations included the staging and evaluation of head and neck cancer, thyroid carcinoma, lung cancer, bronchial carcinoma, breast cancer, lymphoma, liver cancer, colorectal carcinoma, cervical cancer, and prostate cancer. The patients had an average body mass index (BMI) of $24.3 \pm 6.1 \text{ kg m}^{-2}$ and were injected with an activity of $257.8 \pm 43.6 \text{ MBq}$ for ^{18}F -FDG and $329.1 \pm 1.2 \text{ MBq}$ for ^{18}F -Choline. After an uptake period of 60 and 0 min for FDG and FCH administrations, respectively, whole-body PET/CT scanning was performed in continuous bed motion mode from the mid thigh to the vertex of the head with bed speed of 0.7 mm s^{-1} , corresponding

to 3 min per bed position in the conventional step and go acquisition mode. The average acquisition time was 23.2 ± 5.6 min. A whole-body CT scan protocol was performed using CAREdose for PET attenuation correction using the following parameters: 100–120 kVp, 150 mAs, 0.3 s tube rotation, 30.7 mm bed speed per rotation and 5 mm slice thickness.

2.5. MR attenuation map generation

The standard 4-class MRI-based attenuation maps were derived by segmenting CT images of patients into four tissue classes including background air, lung, fat, and non-fat soft tissues. The lungs were semi-automatically segmented using a supervised seeded region growing technique implemented in the ITK-SNAP software (Yushkevich *et al* 2006). Background air was automatically segmented using simple thresholding after removing the CT bed. The fat tissue class was segmented by thresholding CT intensity values between -470 and -53 Hounsfield units (corresponding to PET attenuation coefficients between 0.05 and 0.095 cm^{-1}). The complement of the segmented classes was then defined as soft-tissue class. In this procedure, bones and air pockets are assigned to soft tissue class. Mean attenuation coefficients of 0 , 0.0224 , 0.0864 and 0.0975 cm^{-1} were assigned to background, lungs, fat and non-fat soft tissue classes, respectively. In this work, we used the same mean value of lungs implemented in the MRAC procedure on the Siemens mMR scanner (Siemens Healthcare, Erlangen) (Bezrukov *et al* 2013b). For the lung tissue prior in equation (3), the mean and intra-patient standard deviation of 0.0224 and 0.0107 cm^{-1} were used, respectively. The standard deviation was obtained by fitting a Gaussian to the histogram of lung LACs of 10 CT datasets. The lung set in equation (8) was derived by down-sampling the lung tissue class to the MLAA image reconstruction matrix size. The attenuation map on the mCT is obtained by down-sampling 512×512 CT or 4-class CT images to the resolution of 400×400 , followed by a 4 mm isotropic Gaussian filtering. The estimated MLAA attenuation maps were therefore up-sampled to this resolution and then the lung LACs in the 4-class CT images were replaced by the estimated ones.

2.6. Data analysis

A volume-of-interest (VOI)-based analysis was performed to calculate the relative PET quantification error (bias) with respect to the reference CT-based attenuation correction (CTAC)-PET as follows:

$$\text{Bias} = 100 \times \frac{\text{SUV}_x - \text{SUV}_{\text{CTAC}}}{\text{SUV}_{\text{CTAC}}} \quad (9)$$

where x is the PET image reconstructed using the standard MRAC and constrained MLAA attenuation correction methods. For each patient, circular VOIs were defined on the lungs (upper, middle and lower portions of the left and right lungs) as well as normal tissue regions surrounding the lungs including the liver, descending aorta, myocardium, and 3rd thoracic vertebrae (T3). Moreover, 80% iso-contour VOIs were defined on lesions located in/near the lungs. A total number of 70 lesions were identified. For each VOI, the mean (μ), standard deviation (σ) and root-mean-squared error of the bias ($\sqrt{\mu^2 + \sigma^2}$) was calculated over the 19 patients. The concordance between the SUVs was evaluated using Bland–Altman plots. The statistical significance of differences in SUV bias was also evaluated using the Wilcoxon signed-rank test. The differences were considered statistically significant for p -values less than 0.05. Moreover, the mean and standard deviation of the estimated lung LACs were

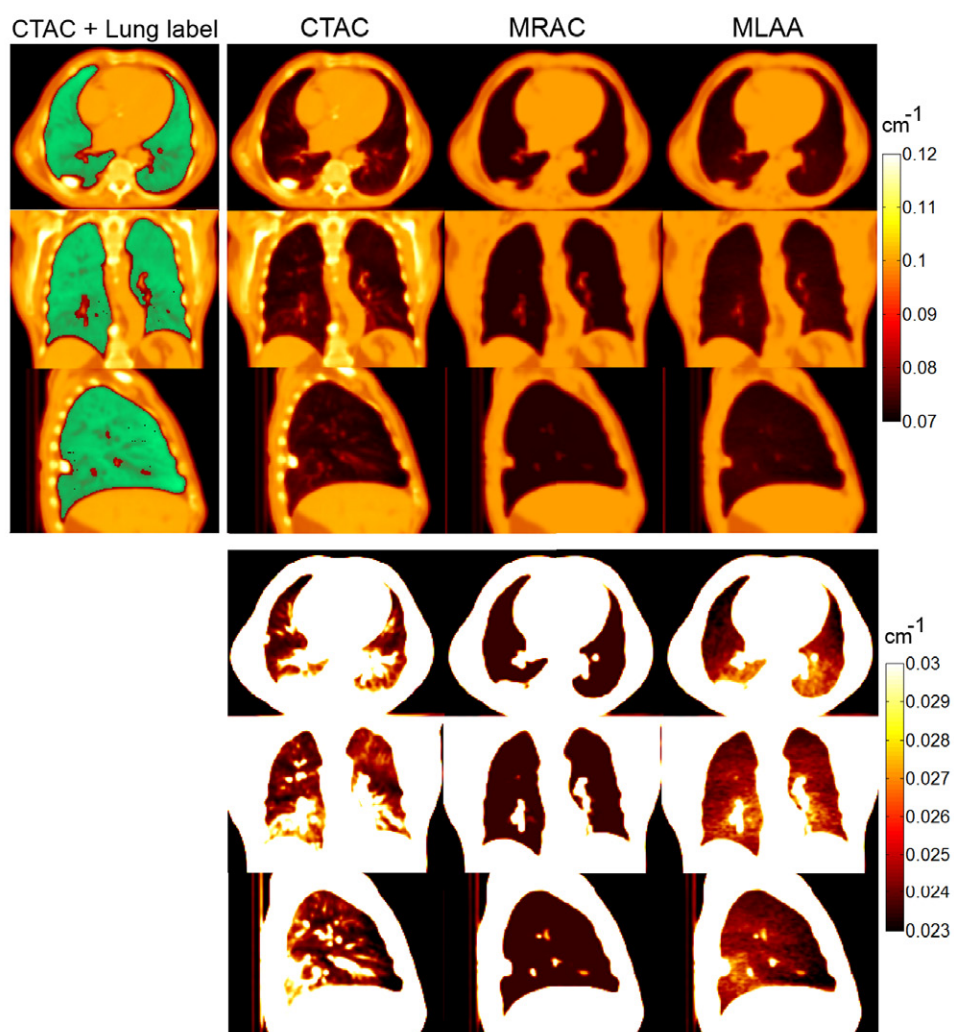


Figure 2. Comparison of the attenuation map derived by the standard 4-class MR-based map (MRAC) with the map obtained by the improved MLAA algorithm and the reference CTAC map in two different display windows. The lung tissue class overlaid on the CTAC map is shown on the left column.

calculated for each patient over all lung voxels and compared with CTAC and MRAC attenuation maps.

3. Results

Figure 2 compares the CT-based attenuation map (CTAC) of a representative patient with the standard 4-class MRAC map and the improved MRAC map over the lungs using the proposed constrained MLAA algorithm in two different display windows. The figure also displays the lung tissue class overlaid on the CTAC image. As shown in the CTAC maps, the lungs in this patient have a congested structure and high density gradients the in antero-posterior and

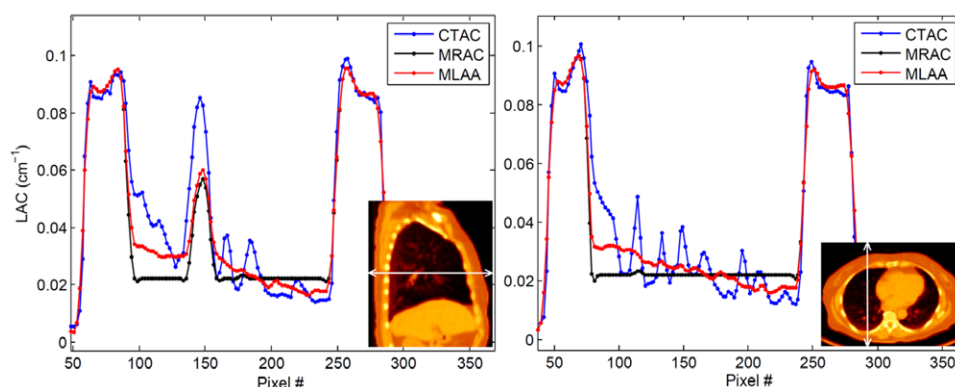


Figure 3. Comparison of attenuation profiles corresponding to the attenuation maps shown in figure 2.

cranio-caudal directions. These patient-specific details are not reflected in the MRAC map, whereas the MLAA algorithm not only can accurately retrieve the lung density gradient in a continuous fashion but also compensates for the segmentation errors in the lung tissue class by increasing the LACs around the partially segmented soft tissue structures (see the sagittal slices). The mean lung LACs of the CTAC, MRAC and MLAA attenuation maps of this dataset (filtered by a 4 mm FWHM Gaussian filter) were 0.0286, 0.0230 and 0.0276 cm^{-1} , respectively.

Figure 3 compares the profiles of MRAC and MLAA attenuation maps with the ground truth CTAC profiles. As can be seen, the MLAA algorithm effectively estimates the attenuation gradients in the same way as the CTAC. However, because of respiratory motion of the lungs during PET acquisition, the MLAA profiles are blurred and do not preserve local details. Moreover, in our improved MLAA algorithm, an MRF smoothing prior is invoked to suppress noisy estimations due to the limited count statistics of the whole-body PET acquisition protocols (equivalent to 3 min per bed).

Table 1 summarizes the mean and standard deviation of lung attenuation coefficients calculated by the three techniques in all 19 patients. The LACs were calculated from the derived attenuation maps, filtered by a 4 mm FWHM Gaussian filter, for all voxels belonging to the lungs. Therefore, the MRAC attenuation maps present with a standard deviation around the predefined LAC of 0.0224 cm^{-1} . In the MLAA attenuation maps of some patients, we observed elevated lung LACs close to the diaphragm and heart due to respiratory-phase mismatch between PET and CT acquisitions and cardiac motion, respectively. This observation was made by the authors through visual inspection of the MLAA attenuation maps. Note that we employed TOF-OSEM algorithm for activity reconstruction. It has been demonstrated that TOF capability can reduce respiratory-phase mismatch artefacts in PET activity maps (Mehranian and Zaidi 2015b). Therefore in some patients, respiratory artefacts were only observable in the MLAA attenuation maps. Figure 4 graphically compares the mean lung LACs of the MRAC and MLAA maps with the reference CTAC map. The results show that overall the emission-based derivation of LACs using the MLAA algorithm follow the trend of the CTAC LACs, except in a few patients, where the estimated LACs are substantially higher than the reference values, while MRAC LACs are almost constant with small deviations from the assigned value of 0.0224 cm^{-1} . The overestimated MLAA LACs in patients No. 2 and 14 should be ascribed to the substantially increased lung LACs induced by respiratory-phase mismatch.

Table 1. Mean and standard deviation of lung attenuation coefficients of 19 clinical datasets calculated using the evaluated AC methods. In the MLAA attenuation maps of some patients, respiratory phase mismatch (RM) and cardiac motion (CM) were observed and reported.

Patient No.	CTAC	MLAA	MRAC	Comment
1	0.0303 ± 0.0100	0.0351 ± 0.0055	0.0221 ± 0.0018	
2	0.0209 ± 0.0064	0.0279 ± 0.0049	0.0224 ± 0.0018	RM
3	0.0286 ± 0.0134	0.0276 ± 0.0068	0.0230 ± 0.0045	
4	0.0253 ± 0.0089	0.0284 ± 0.0053	0.0227 ± 0.0037	RM and CM
5	0.0329 ± 0.0105	0.0287 ± 0.0057	0.0230 ± 0.0043	RM
6	0.0301 ± 0.0085	0.0274 ± 0.0046	0.0225 ± 0.0022	CM
7	0.0261 ± 0.0127	0.0250 ± 0.0035	0.0225 ± 0.0023	
8	0.0220 ± 0.0107	0.0242 ± 0.0053	0.0225 ± 0.0014	
9	0.0264 ± 0.0068	0.0272 ± 0.0043	0.0226 ± 0.0014	RM
10	0.0252 ± 0.0045	0.0245 ± 0.0016	0.0225 ± 0.0012	
11	0.0250 ± 0.0145	0.0254 ± 0.0053	0.0231 ± 0.0010	RM
12	0.0293 ± 0.0114	0.0287 ± 0.0061	0.0232 ± 0.0024	RM and CM
13	0.0256 ± 0.0074	0.0249 ± 0.0028	0.0224 ± 0.0010	
14	0.0229 ± 0.0097	0.0282 ± 0.0055	0.0222 ± 0.0016	RM
15	0.0207 ± 0.0071	0.0232 ± 0.0032	0.0225 ± 0.0014	
16	0.0198 ± 0.0063	0.0243 ± 0.0031	0.0221 ± 0.0001	RM
17	0.0275 ± 0.0086	0.0280 ± 0.0065	0.0233 ± 0.0056	
18	0.0203 ± 0.0048	0.0241 ± 0.0025	0.0225 ± 0.0011	
19	0.0246 ± 0.0056	0.0240 ± 0.0024	0.0226 ± 0.0017	

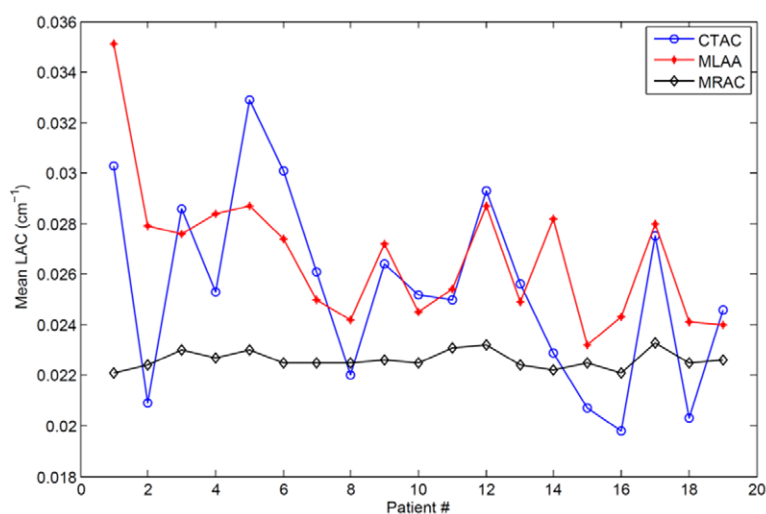


Figure 4. Comparison of the mean lung LACs of MRAC and MLAA attenuation maps with the reference CTAC map in all 19 patients.

Figure 5 shows PET and CT images of a patient having a liver lesion and respiratory PET/CT mismatch, together with the MRAC and MLAA attenuation maps using the lung display window. The MLAA attenuation map shows the increase of lung LACs in the vicinity of the right diaphragm, implying the presence of respiratory mismatch, which is confirmed

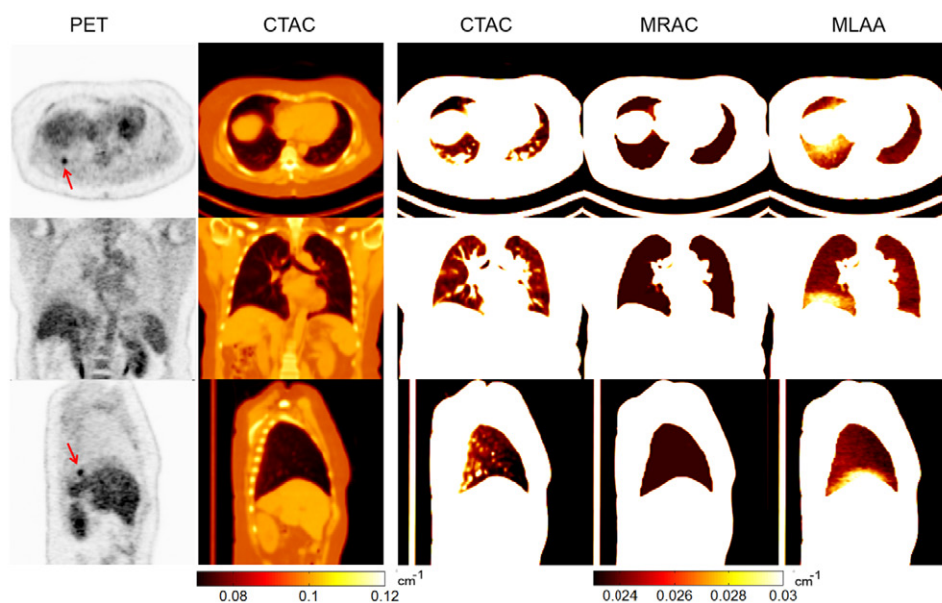


Figure 5. PET and CT images of a patient having a liver lesion and respiratory phase mismatch between CT and PET acquisitions, together with the MRAC and MLAA attenuation maps in different display windows.

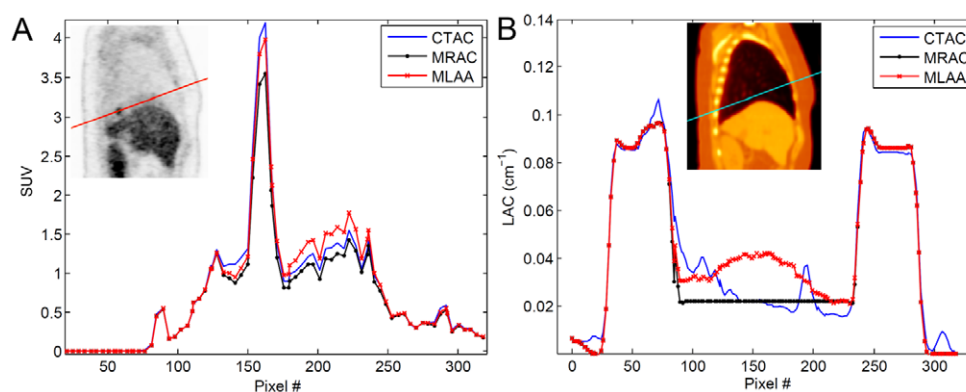


Figure 6. Comparison of activity (A) and attenuation (B) profiles of the dataset shown in figure 5 over the liver lesion.

on the sagittal view of the CTAC PET image where the top rim of the liver shows an abrupt decrease of activity. As can be seen in the sagittal slices, the MLAA attenuation map can also effectively predict the antero-posterior density gradient of the lungs in this patient dataset. Figure 6 further illustrates the performance of the proposed MLAA algorithm by comparing the activity and attenuation profiles of the dataset shown in figure 5. The activity profiles show an underestimation of the lesion's SUV by the standard MRAC method, while MLAA was able to considerably increase the lesion's SUV values toward those obtained by CTAC PET images. Over the liver, there is a considerable increase of tracer uptake in the MLAA PET image, which is brought about by the corresponding increased LACs, as shown in figure 6(B). Note that the SUV values of the MLAA are lower than those of the CTAC over the lesion. This

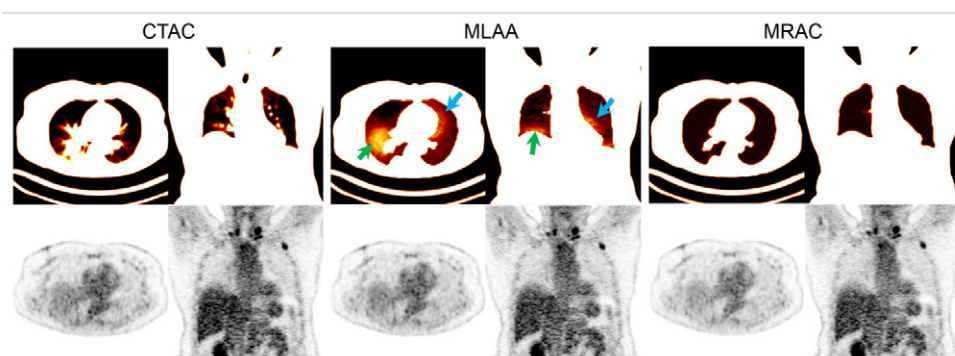


Figure 7. Top: the attenuation maps of a patient with respiratory and cardiac motion in lung display window. Bottom: qualitative comparison of the corresponding attenuation corrected PET images.

Table 2. Relative PET quantification errors [mean \pm SD, (RMSE)] of MRAC and MLAA methods in different regions of interest with CTAC serving as reference.

ROI	MRAC	MLAA	P-value
Upper left lung	-4.1 ± 6.7 (7.9)	-1.0 ± 7.0 (7.0)	< 0.0001
Middle left lung	-2.9 ± 6.2 (6.9)	0.4 ± 5.5 (5.6)	< 0.0001
Lower left lung	-8.8 ± 5.5 (10.4)	-3.2 ± 5.3 (6.2)	< 0.0001
Upper right lung	-2.6 ± 7.2 (7.7)	0.3 ± 7.4 (7.4)	< 0.0001
Middle right lung	-4.5 ± 7.6 (8.9)	0.4 ± 6.3 (6.3)	< 0.0001
Lower right lung	-8.2 ± 7.1 (10.9)	-1.8 ± 6.0 (6.3)	< 0.0001
Total lungs	-5.2 ± 7.1 (8.8)	-0.8 ± 6.3 (6.4)	< 0.0001
Liver	-6.1 ± 2.4 (6.6)	-5.4 ± 2.1 (5.7)	< 0.0005
Aorta	-7.1 ± 4.8 (8.6)	-4.2 ± 3.5 (5.5)	< 0.0001
Myocardium	-9.5 ± 4.3 (10.4)	-5.7 ± 3.2 (6.5)	< 0.0001
T3 vertebra	-14.1 ± 2.5 (14.3)	-12.0 ± 2.1 (12.2)	< 0.0001
Lesions	-6.1 ± 6.7 (9.1)	-3.3 ± 4.7 (5.7)	< 0.0001

should be ascribed to the fact that this soft-tissue lesion was mis-segmented as can be seen on the sagittal images of figure 5. This result highlights the ability of the MLAA algorithm to compensate for lung segmentation errors.

Figure 7 shows the attenuation maps of another patient presenting with respiratory and cardiac motion together with their corresponding PET images. The visual inspection of the MLAA attenuation map shows the presence of cardiac and respiratory motion and the potential of the emission-based algorithm to produce improved attenuation maps. However, the qualitative comparison of the PET images shows that the various AC methods result in similar lesion detectability and conspicuity in this dataset.

The quantitative PET accuracy of the proposed MLAA algorithm was further evaluated in all patient datasets using VOI-based analysis in comparison with the standard MRAC and CTAC methods. Table 2 summarizes the mean, standard deviation (SD) and root-mean-squared error (RMSE) of SUV_{mean} bias in VOIs defined on the upper (U), middle (M) and lower (L) regions of the left (L) and right (R) lungs, as well as the adjacent normal tissue regions and lesions. Figure 8(A) compares the bias results in the lungs. In this figure, the markers show the mean of the bias in each VOI, whereas the horizontal bars and vertical boxes indicate the mean

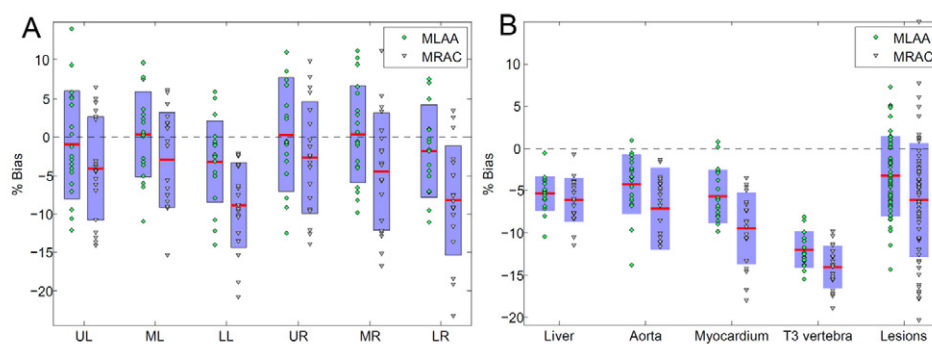


Figure 8. Relative SUV errors of MRAC and MLAA attenuation correction methods in (A) six lung regions and (B) normal tissues close to the lungs with reference CTAC PET images. Means and one-standard deviations are indicated by the horizontal bars and vertical boxes, respectively.

and standard deviations of the bias between VOIs in each region. The results demonstrate that the MLAA algorithm generally gives rise to a reduced mean bias over all regions of the lungs, especially in the lower parts, since normally there is a cranio-caudal density gradient in the lungs, with increased LACs towards the base of the lungs. For all VOIs defined in the lungs ($n = 114$), the MRAC method resulted in an underestimation of tracer uptake of $-5.2 \pm 7.1\%$ with a RMES of 8.8%, while the MLAA method yielded an error of $-0.8 \pm 6.3\%$ with a RMSE of 6.4% (table 2). Although this algorithm decreases the mean of the bias toward zero, the standard deviation of the bias is not remarkably reduced, which should be ascribed to the sub-optimal regularization parameters and number of iterations used. However, the statistical analysis, revealed a significant difference between the performances of the different attenuation correction methods.

Figure 8(B) illustrates the impact of the emission-based estimation of lung attenuation coefficients on quantification errors in adjacent normal organs to the lungs including the liver, aorta, myocardium, 3rd thoracic vertebra; as well as the identified lesions in all patients. As presented in table 2, the results show a statistically significant reduction of the bias in neighbouring organs, especially in the myocardium and aorta. The results also show that the attenuation coefficients of the lung can impact the PET bias over the vertebra, where the LACs of bones have been substituted by those of soft tissue in both MRAC and MLAA attenuation maps. Nonetheless, the MLAA reduced the mean of bone bias from -14.1 to -12.0% over all patients. For the VOIs defined in the lesions ($n = 70$), the MRAC method resulted in an underestimation of $-6.1 \pm 6.7\%$ with a RMES of 9.1%, which was reduced by the MLAA method to $-3.3 \pm 4.7\%$ with a RMSE of 5.7%. Most of the lesions were mediastinal lymph node involvements, for which the mis-segmentation of soft tissue structures, such as pulmonary vessels and bronchioles, into the lung tissue class is unavoidable for current standard MR pulse sequences.

The AC methods were further analyzed in terms of SUV concordance with the reference CTAC technique. Figure 9 shows the Bland–Altman plots for the lung VOIs and malignant lesions. As can be seen, both MRAC and MLAA methods show a systematic bias in the SUV estimates of lung tissues and lesions. However, consistent with the results presented in table 2, the mean of the bias (horizontal lines) is reduced by the MLAA attenuation correction method.

The performance of the proposed MLAA algorithm depends on the involved parameters, such as the number of iterations and subsets, the magnitude of regularization parameters, β and

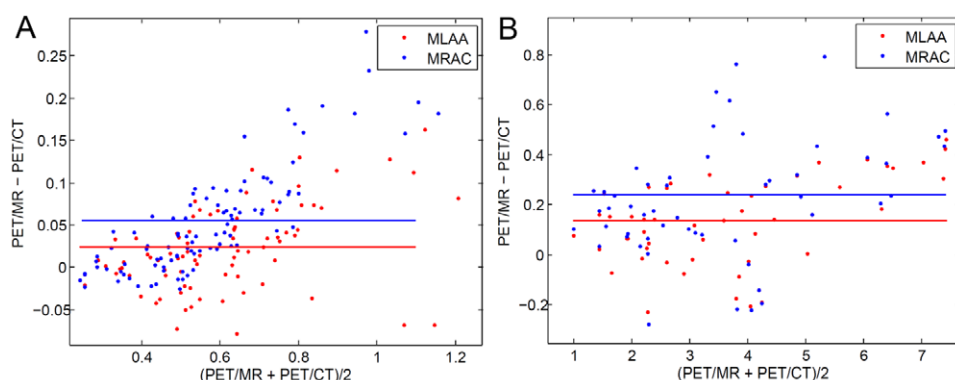


Figure 9. Bland–Altman plots of SUVmean estimated using MRAC and MLAA PET images with respect to CTAC PET images for (A) all lung VOIs and (B) all lesions.

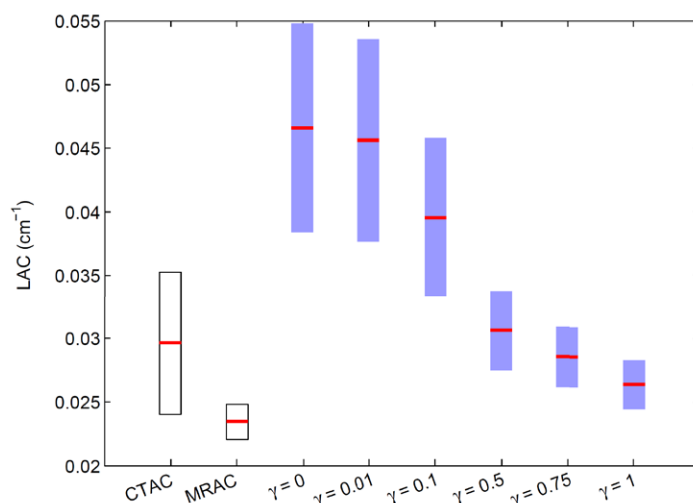


Figure 10. Impact of the γ weighting parameter of the lung tissue preference prior on the performance of the proposed constrained MLAA algorithm. The horizontal bars and vertical boxes indicate the mean and standard deviation of lung attenuation coefficients for patient no. 11 (see table 2).

γ , and the step size α of the MLTR algorithm. In this work, we heuristically optimized these parameters for a few patient datasets and employed them for all 19 patients. The Gaussian tissue preference prior is the essential element of the proposed algorithm. In fact, this algorithm derives the lung LACs in an interval between the standard 4-class MRAC method and the original MLAA algorithm, depending on the γ weighting factor. Figure 10 compares the mean \pm half-standard deviation of the estimated lung LACs using the MLAA algorithm with the MRAC and reference CTAC techniques for patient No. 11 (see table 1) with the weighting factor increasing from zero (corresponding to the original MLAA) to 1. The lung tissue prior, parameterized over a patient population, in fact penalizes the large deviation of the attenuation coefficients from the expected values, depending on the γ parameter. As shown in figure 10, very low values of γ reduce the algorithm to the original MLAA, which results in a high

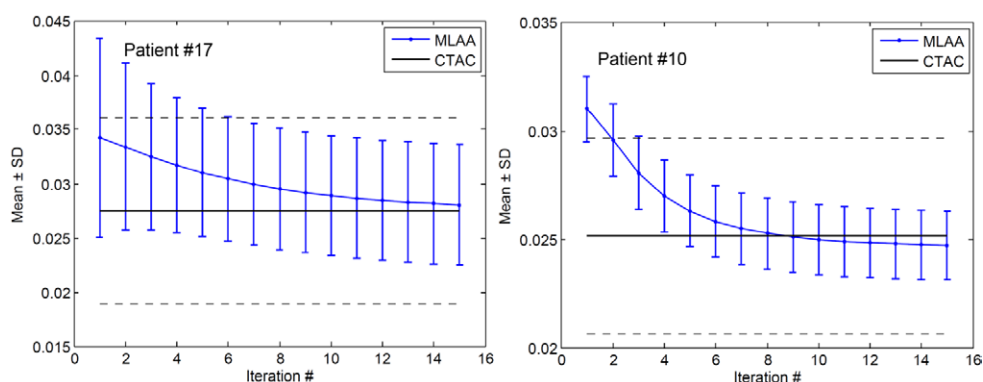


Figure 11. Mean and standard deviation (error bars) of lung LACs in two patients as a function of iteration number. The horizontal solid and dashed lines represent the mean \pm standard deviation of CTAC lung LACs, respectively.

error in estimating the mean LACs. This should be attributed to out-of-field accidental coincidences, error propagation into the lungs from adjacent regions (because bones are replaced by soft tissue in the 4-class MRAC maps) and the still unsolved scaling problem of the MLAA algorithm. On the other hand, for very large values of γ , the proposed MLAA algorithm is reduced to the standard MRAC method, which guarantees a safe-failure method. We nearly optimized this parameter for a few clinical studies and employed it for the rest of patient datasets. As mentioned earlier, we chose $\gamma = 0.75$, $\beta = 80$, $\alpha = 1.5$ for all patient datasets. Our preliminary results showed that there is greater flexibility in selecting the last two parameters than the first one. Finally, as shown in figure 11, we obtained the 15 global iterations as a near-to-optimal number of iterations for a few datasets and utilized it for all other datasets.

4. Discussion

Recently, TOF-PET technology has been implemented on clinical PET scanners with the aim of improving lesion detectability and image quality, as well as reducing acquisition time and/or patient's administrated activity (Conti 2011). With the advent of TOF-PET scanners, the simultaneous maximum likelihood estimation of activity and attenuation has regained popularity (Rezaei *et al* 2012). Emission-based attenuation correction strategies are particularly promising in PET/MR imaging for overcoming the quantification errors induced by conventional segmentation-based AC methods (Salomon *et al* 2011). Based on our previous work (Mehranian and Zaidi 2015a), we report on the use of a constrained MLAA algorithm for patient-specific emission-based estimation of lung attenuation coefficients with the aim of improving existing 4-class MRAC methods.

Among the different tissue classes defined in segmentation-based AC methods, the lungs have the largest inter-patient LAC variability with a standard deviation of 0.004 cm^{-1} (Keereman *et al* 2011, Schulz *et al* 2011), which is similar to the standard deviation of mean CTAC attenuation coefficients (table 1). This standard deviation is about 20 times higher than that of soft tissue (Schulz *et al* 2011). Therefore, if patient-specific lung LACs are not considered in MRAC maps, PET quantification errors up to 26% might result (Keereman *et al* 2011). In (Martinez-Moller *et al* 2009) and (Arabi *et al* 2015), a LAC of 0.018 cm^{-1} was assigned to the lungs, resulting in PET quantification bias of $1.9 \pm 2.3\%$ and $-0.5 \pm 13.3\%$ in lung lesions and lung normal tissues, respectively. In earlier studies, a linear attenuation coefficient

of 0.024 cm^{-1} was assigned to the lungs, resulting in relative errors of $13.5 \pm 10.7\%$ (Hofmann *et al* 2011) and $7.7 \pm 3.0\%$ (Marshall *et al* 2013). Ouyang *et al* (Ouyang *et al* 2013) reported a relative error of $4.4 \pm 14.4\%$ for SUV estimates of the lungs when using lung LACs of 0.0276 cm^{-1} . Our results exhibited an average SUV bias of $-5.2 \pm 7.1\%$ when using lung LACs of 0.0224 cm^{-1} in the standard MRAC method. The discrepancy between the reported errors should be attributed to the assignment of different lung LACs and the usage of different lung segmentation algorithms. The results presented in table 1 and figure 4 demonstrate that the MLAA algorithm is generally in agreement with patient-specific lung attenuation coefficients determined using the CTAC method, except in a few patients, where severe respiratory motion and elevated LACs in the posterior regions of the lungs were observed. Overall, the proposed AC method reduced the bias in the lung tissue to $-0.8 \pm 6.3\%$. The results presented in table 2 indicate that the MLAA technique noticeably outperformed the MRAC method in the lower lobes of the lungs, where the lung attenuation coefficients are commonly higher than in the upper lobes. In these regions, the MRAC and MLAA methods resulted in an average bias of $-8.5 \pm 6.3\%$ and $-2.5 \pm 5.6\%$, respectively. These results along with those shown in figures 2, 3 and 5 demonstrate that the proposed AC method can fairly capture the voxel-wise intra-patient variability of lung LACs.

In the case of respiratory mismatch between the reference CTAC and PET images, only MLAA-AC method shows increased attenuation values in the vicinity of the diaphragm. Therefore, in these cases, the MLAA approach overestimates the activity with respect to the reference CTAC method. However, the LACs derived from CTAC do not reflect the actual ones. Regarding the evaluation of the AC methods, we performed a class-wise analysis to provide a global metric for the estimated attenuation coefficients over the whole lung (table 1). In this case, the differences due to respiratory mismatch between the proposed approach and the CTAC method are not distinguishable. However, according to our experience the outperformance of MLAA over MRAC in the lower part of the lungs is mainly due to the fact that the MLAA algorithm retrieves well the lung density gradients. In the SUV evaluations, we used a VOI-based analysis. The placement of a single VOI in the lower portions of the lungs partly excludes the SUV differences due to respiratory mismatch between the proposed approach and the CTAC method.

Among MRI-guided AC methods, atlas-based registration and pattern recognition (AT&PR) methods predict continuous LACs, thus considering intra-patient variability. The technique proposed by Hofmann *et al* (Hofmann *et al* 2011) incorporates the local structures of MR images and co-registered CT atlases into Gaussian process regression (GPR) kernels to predict patient-specific attenuation maps. In spite of considerable SUV bias reduction in soft-tissue and bony structures, this method exhibited large bias in the lungs as much as the standard 4-class MRAC method. In fact, lung tissues have low proton densities and short transverse relaxation times. As such, lung MR intensities in standard MR sequences are low and do not provide sufficient information to easily distinguish lung density variations. Recently, Arabi and Zaidi embedded the correlation between lung volume and lung mean LACs into the GPR kernels and showed that their improved AT and PR method reduces the lung SUV bias from 8.9 to 4.1% (Arabi and Zaidi 2014). Ultra-short echo time (UTE) MR pulse sequences have also been investigated for the detection and visualization of lung parenchyma density to improve lung segmentation and bone depiction (Zeimpekis *et al* 2014). However, UTE pulse sequences are timing-consuming and sensitive to magnetic field inhomogeneities and are therefore, not yet clinically feasible in whole-body MRAC.

Although the mean lung LACs are low compared to other tissue classes, the lung's volume is large and therefore non patient-specific and inaccurate assignment of attenuation values to the lungs can affect the quantification accuracy of the neighbouring organs and lesions. The

MLAA algorithm can reduce SUV quantification errors in different neighbouring tissues by deriving patient-specific lung LACs (table 2, figure 8). In particular, it was found that for lesions in/close to the lungs, this algorithm can reduce the bias from -6.1 to -3.3% . As shown in figure 6, the algorithm is promising especially in terms of reducing the adverse effect of respiratory phase mismatch between PET and MR on the quantification of liver lesions uptake (Mehranian and Zaidi 2015c).

Over 114 VOIs defined in the lungs, the MRAC and MLAA methods resulted in maximum SUV underestimation of -23.3 and -14.0% , and maximum SUV overestimation of 11.1 and 15.0% , respectively. As can be seen in figure 8(A), the MLAA algorithm did not noticeably reduce the standard deviation of the errors compared to the MRAC method. This should be attributed to the potentially sub-optimal weighting factor of the Gaussian tissue prior used in our MLAA algorithm, the intrinsic limitations and count-dependency of the emission-based AC methods and the contribution of out-of-field accidental coincidences. The latter is more prominent in the work of (Berker *et al* 2012), where high SUV errors were observed on Monte Carlo simulated PET/CT datasets. In contrast, our proposed MLAA method showed a promising performance and demonstrated the potential and benefits of emission-based AC methods. The primary advantage of our method compared to Berker *et al* is the derivation of continuous lung attenuation values that can not only capture the lung density gradients but also fairly compensate for respiratory mismatch, cardiac motion and segmentation errors. The shortcoming of our voxel-wise estimation of LACs compared to their class-wise approach is the higher noise and possibly the lower convergence rate of the algorithm. To tackle these problems, we incorporated a MRF smoothing prior in the algorithm and initialized it with the standard 4-class MRAC map. Our simplified MLAA algorithm is in essence similar to the one proposed by (Nuyts *et al* 2013) for the compensation of arm truncation of MRAC maps, except that they used a bi-modal Gaussian intensity prior to favour the separation of soft tissue attenuation values from air. However, this prior is not twice continuously differentiable and might result in instability of the solution.

To this end, it is worth to recognize the limitations of this study and highlight future directions for improving the performance of the proposed algorithm. Emission-based estimation of attenuation coefficients depends on the biodistribution of the tracer in the body. In fact, the attenuation map cannot be completely estimated for LORs that are out of the support of the activity distribution, especially for specific tracers that have a localized uptake. In our patient population, the clinical studies encompassed ^{18}F -FDG ($n = 17$) and ^{18}F -Choline ($n = 2$) scans. For the bed positions of interest to us, the biodistribution of ^{18}F -Choline is almost similar to that of ^{18}F -FDG, except in the brain (Schillaci *et al* 2010). Therefore, our assertion that both tracers support well the estimation of attenuation is justified. However, whether the local differences in uptake pattern influences the estimated attenuation values remains to be demonstrated. As shown in figure 10, the performance of our method depends highly on the selected γ parameter. The choice of the hyper-parameters for MAP image reconstruction is usually not straightforward. In this work, we nearly optimized this parameter for a few patient datasets (3–5) by trial and error and used it for all other patient datasets. Although this parameter selection approach allowed for the evaluation of the method over a reasonable patient population, the selected parameter might not be optimal for all datasets, especially in cases where it is not high enough to penalize the high LAC deviations induced by error propagation from neighbouring tissue classes and out-of-field accidental coincidences. An adaptive selection of this parameter can be achieved using discrete data consistency conditions (Panin *et al* 2004) or hierarchical Bayesian approach for its iterative estimation (Kang and Katsaggelos 1995), which will be investigated in future work. Similarly, we heuristically selected the update schedule of the MLAA algorithm with a fixed number of global iterations for all patients.

Future work will focus on defining a stopping criterion based on decreasing consistency error or Kullback–Leibler distance.

5. Conclusion

The proposed constrained MLAA algorithm provides a promising and feasible method for deriving patient-specific lung attenuation maps in TOF PET/MR imaging. It was demonstrated that this algorithm retrieves the lung density gradients and can compensate for respiratory motion artefacts. Our results showed that the conventional 4-class MRAC method resulted in average SUV errors of -5.2 and -6.1% in normal lung tissues and lesions, respectively, in/near the lungs. Emission-based estimation of lung LACs using the MLAA algorithm reduced the errors to -0.8 and -3.3% , respectively. In conclusion, the results achieved using the proposed algorithm suggest that emission-based estimation of lung attenuation coefficients in the MLAA framework using lung tissue preference priors show promise for attenuation correction of PET/MR imaging.

Acknowledgment

This work was supported in part by the Swiss National Science Foundation under Grant SNSF 31003A-149957 and the Indo-Swiss Joint Research Programme ISJRP 138866.

References

- Arabi H, Rager O, Alem A, Varoquaux A, Becker M and Zaidi H 2015 Clinical assessment of MR-guided 3-class and 4-class attenuation correction in PET/MR *Mol. Imaging Biol.* **17** 264–76
- Arabi H and Zaidi H 2014 MRI-based pseudo-CT generation using sorted atlas images in whole-body PET/MRI *IEEE Nuclear Science Symp. and Medical Imaging Conf. (NSS/MIC) (Seattle, WA, USA)* in press
- Berker Y, Salomon A, Kiessling F and Schulz V 2012 Lung attenuation coefficient estimation using Maximum Likelihood reconstruction of attenuation and activity for PET/MR attenuation correction *Proc. IEEE Nuclear Science Symp. and Medical Imaging Conf. (NSS/MIC)* pp 2282–4
- Bezrukov I, Mantlik F, Schmidt H, Scholkopf B and Pichler B J 2013a MR-based PET attenuation correction for PET/MR imaging *Semin. Nucl. Med.* **43** 45–59
- Bezrukov I, Schmidt H, Mantlik F, Schwenzler N, Brendle C, Scholkopf B and Pichler B J 2013b MR-based attenuation correction methods for improved PET quantification in lesions within bone and susceptibility artifact regions *J. Nucl. Med.* **54** 1768–74
- Bronnikov A V 2000 Reconstruction of attenuation map using discrete consistency conditions *IEEE Trans. Med. Imaging* **19** 451–62
- Clinthorne N H, Fessler J A, Hutchins G D and Rogers W L 1991 Joint maximum likelihood estimation of emission and attenuation densities in PET *Conf. Record of the IEEE Nuclear Science Symp. and Medical Imaging Conf. (SantaFe, CA, 2–9 November 1991)* pp 1927–32
- Conti M 2011 Focus on time-of-flight PET: the benefits of improved time resolution *Eur. J. Nucl. Med. Mol. Imaging* **38** 1147–57
- Defrise M, Rezaei A and Nuyts J 2012 Time-of-flight PET data determine the attenuation sinogram up to a constant *Phys. Med. Biol.* **57** 885–99
- Disselhorst J A, Bezrukov I, Kolb A, Parl C and Pichler B J 2014 Principles of PET/MR Imaging *J. Nucl. Med.* **55** 2S–10S
- Fessler J A, Ficaro E P, Clinthorne N H and Lange K 1997 Grouped-coordinate ascent algorithms for penalized-likelihood transmission image reconstruction *IEEE Trans. Med. Imaging* **16** 166–75
- Gattinoni L, Pelosi P, Vitale G, Pesenti A, D'Andrea L and Mascheroni D 1991 Body position changes redistribute lung computed-tomographic density in patients with acute respiratory failure *Anesthesiology* **74** 15–23

- Hofmann M, Bezrukov I, Mantlik F, Aschoff P, Steinke F, Beyer T, Pichler B J and Scholkopf B 2011 MRI-based attenuation correction for whole-body PET/MRI: quantitative evaluation of segmentation- and Atlas-based methods *J. Nucl. Med.* **52** 1392–9
- Hofmann M, Steinke F, Scheel V, Charpiat G, Farquhar J, Aschoff P, Brady M, Scholkopf B and Pichler B J 2008 MRI-based attenuation correction for PET/MRI: a novel approach combining pattern recognition and Atlas registration *J. Nucl. Med.* **49** 1875–83
- Hu Z *et al* 2010 MR-based attenuation correction for a whole-body PET/MR system *IEEE Nuclear Science Symp. Conf. Record (Knoxville, TN, 30 October–6 November 2010)* pp 2119–22
- Johansson A, Karlsson M and Nyholm T 2011 CT substitute derived from MRI sequences with ultrashort echo time *Med. Phys.* **38** 2708–14
- Kacperski K 2011 Attenuation correction in SPECT without attenuation map *Proc. IEEE Nuclear Science Symp. and Medical Imaging Conf. (NSS/MIC) (Valencia, 23–29 October 2011)* pp 3820–2
- Karimi R, Tornling G, Forsslund H, Mikko M, Wheelock A, Nyren S and Skold C M 2014 Lung density on high resolution computer tomography (HRCT) reflects degree of inflammation in smokers *Respir. Res.* **15** 23
- Keereman V, Holen R V, Mollet P and Vandenberghe S 2011 The effect of errors in segmented attenuation maps on PET quantification *Med. Phys.* **38** 6010–9
- Kim J H, Lee J S, Song I C and Lee D S 2012 Comparison of segmentation-based attenuation correction methods for PET/MRI: evaluation of bone and liver standardized uptake value with oncologic PET/CT data *J. Nucl. Med.* **53** 1878–82
- Krol A, Bowsler J E, Manglos S H, Feiglin D H, Tornai M P and Thomas F D 2001 An EM algorithm for estimating SPECT emission and transmission parameters from emissions data only *IEEE Trans. Med. Imaging* **20** 218–32
- Landmann M, Reske S N and Glatting G 2002 Simultaneous iterative reconstruction of emission and attenuation images in positron emission tomography from emission data only *Med. Phys.* **29** 1962–7
- Lonn A R and Wollenweber S D 2012 Estimation of mean lung attenuation for use in generating PET attenuation maps *Proc. IEEE Nuclear Science Symp. and Medical Imaging Conf. (NSS/MIC) (Anaheim, CA, 27 October–3 November 2012)* pp 3017–8
- Madsen M T and Lee J R 1999 Emission based attenuation correction of PET images of the thorax *Proc. IEEE Nuclear Science Symp. (Seattle, WA)* ed E J Hoffman pp 967–71
- Marshall H R, Patrick J, Laidley D, Prato F S, Butler J, Theberge J, Thompson R T and Stodilka R Z 2013 Description and assessment of a registration-based approach to include bones for attenuation correction of whole-body PET/MRI *Med. Phys.* **40** 082509
- Marshall H R, Prato F S, Deans L, Theberge J, Thompson R T and Stodilka R Z 2012 Variable lung density consideration in attenuation correction of whole-body PET/MRI *J. Nucl. Med.* **53** 977–84
- Martinez-Moller A, Souvatzoglou M, Delso G, Bundschuh R A, Chefd'hotel C, Ziegler S I, Navab N, Schwaiger M and Nekolla S G 2009 Tissue classification as a potential approach for attenuation correction in whole-body PET/MRI: evaluation with PET/CT data *J. Nucl. Med.* **50** 520–6
- Mehranian A and Zaidi H 2015a Joint estimation of activity and attenuation in whole-body TOF PET/MRI using constrained Gaussian mixture models *IEEE Trans. Med. Imaging* in press
- Mehranian A and Zaidi H 2015b Impact of time-of-flight PET on quantification errors in MRI-based attenuation correction *J. Nucl. Med.* **56** 635–41
- Mehranian A and Zaidi H 2015c Clinical evaluation of emission- and segmentation-based MR-guided attenuation correction in whole-body time-of-flight PET/MRI *J. Nucl. Med.* **56** 877–83
- Mollet P, Keereman V, Bini J, Izquierdo-Garcia D, Fayad Z A and Vandenberghe S 2014 Improvement of attenuation correction in time-of-flight PET/MR imaging with a positron-emitting source *J. Nucl. Med.* **55** 329–36
- Kang M G and Katsaggelos A K 1995 General choice of the regularization functional in regularized image restoration *IEEE Trans. Image Process.* **4** 594–602
- Navalpakkam B K, Braun H, Kuwert T and Quick H H 2013 Magnetic resonance-based attenuation correction for PET/MR hybrid imaging using continuous valued attenuation maps *Invest. Radiol.* **48** 323–32
- Nuyts J, Bal G, Kehren F, Fenchel M, Michel C and Watson C 2013 Completion of a truncated attenuation image from the attenuated PET emission data *IEEE Trans. Med. Imaging* **32** 237–46
- Nuyts J, De Man B, Dupont P, Defrise M, Suetens P and Mortelmans L 1998 Iterative reconstruction for helical CT: a simulation study *Phys. Med. Biol.* **43** 729–37

- Nuyts J, Dupont P, Stroobants S, Beninck R, Mortelmans L and Suetens P 1999 Simultaneous maximum *a posteriori* reconstruction of attenuation and activity distributions from emission sinograms *IEEE Trans. Med. Imaging* **18** 393–403
- Ouyang J, Chun S Y, Petibon Y, Bonab A A, Alpert N and El Fakhri G 2013 Bias atlases for segmentation-based PET attenuation correction using PET-CT and MR *IEEE Trans. Nucl. Sci.* **60** 3373–82
- Panin V Y, Aykac M and Casey M E 2013 Simultaneous reconstruction of emission activity and attenuation coefficient distribution from TOF data, acquired with external transmission source *Phys. Med. Biol.* **58** 3649–69
- Panin V Y, Kehren F, Hamill J and Michel C 2004 Application of discrete data consistency conditions for selecting regularization parameters in PET attenuation map reconstruction *Phys. Med. Biol.* **49** 2425–36
- Rezaei A, Defrise M, Bal G, Michel C, Conti M, Watson C and Nuyts J 2012 Simultaneous reconstruction of activity and attenuation in time-of-flight PET *IEEE Trans. Med. Imaging* **31** 2224–33
- Rezaei A, Defrise M and Nuyts J 2014 ML-reconstruction for TOF-PET with simultaneous estimation of the attenuation factors *IEEE Trans. Med. Imaging* **33** 1563–72
- Robinson P J and Kreef L 1979 Pulmonary tissue attenuation with computed tomography: comparison of inspiration and expiration scans *J. Comput. Assist. Tomogr.* **3** 740–8
- Rothfuss H, Panin V, Moor A, Young J, Hong I, Michel C, Hamill J and Casey M 2014 LSO background radiation as a transmission source using time of flight *Phys. Med. Biol.* **59** 5483–500
- Salomon A, Goedicke A and Aach T 2009 Simultaneous reconstruction of activity and attenuation in multi-modal ToF-PET *Proc. 10th Int. Meeting on Fully 3D Image Reconstruction in Radiology and Nuclear Medicine (Fully3D) (Beijing, China, 5–10 September 2009)* pp 339–42
- Salomon A, Goedicke A, Schweizer B, Aach T and Schulz V 2011 Simultaneous reconstruction of activity and attenuation for PET/MR *IEEE Trans. Med. Imaging* **30** 804–13
- Schillaci O, Calabria F, Tavolozza M, Ciccio C, Carlini M, Caracciolo C R, Danieli R, Orlacchio A and Simonetti G 2010 ¹⁸F-choline PET/CT physiological distribution and pitfalls in image interpretation: experience in 80 patients with prostate cancer *Nucl. Med. Commun.* **31** 39–45
- Schreibmann E, Nye J A, Schuster D M, Martin D R, Votaw J and Fox T 2010 MR-based attenuation correction for hybrid PET-MR brain imaging systems using deformable image registration *Med. Phys.* **37** 2101–9
- Schulz V *et al* 2011 Automatic, three-segment, MR-based attenuation correction for whole-body PET/MR data *Eur. J. Nucl. Med. Mol. Imaging* **38** 138–52
- Torigian D A, Zaidi H, Kwee T C, Saboury B, Udupa J K, Cho Z-H and Alavi A 2013 PET/MR Imaging: technical aspects and potential clinical applications *Radiology* **267** 26–44
- Watson C C 2014 Supplemental transmission method for improved PET attenuation correction on an integrated MR/PET *Nucl. Instrum. Methods A* **734** 191–5 (Part B)
- Welch A *et al* 1998 Attenuation correction in PET using consistency information *IEEE Trans. Nucl. Sci.* **45** 3134–41
- Yushkevich P A, Piven J, Hazlett H C, Smith R G, Ho S, Gee J C and Gerig G 2006 User-guided 3D active contour segmentation of anatomical structures: significantly improved efficiency and reliability *Neuroimage* **31** 1116–28
- Zaidi H 2007 Is MRI-guided attenuation correction a viable option for dual-modality PET/MR imaging? *Radiology* **244** 639–42
- Zeimpekis K, Delso G, Wiesinger F, Veit-Haibach P, von Schulthess G and Grimm R 2014 Investigation of 3D UTE MRI for lung PET attenuation correction [abstract] *J. Nucl. Med.* **55** 2103